JGR Solid Earth

RESEARCH ARTICLE
10.1029/2019JB018796

Precision Seismic Monitoring and Analysis at Axial Seamount Using a Real-Time Double-Difference System

F. Waldhauser[1], W. S. D. Wilcock[2], M. Tolstoy[1], C. Baillard[2], Y. J. Tan[1], and D. P. Schaff[1]

[1]Lamont-Doherty Earth Observatory, Columbia University, Palisades, NY, USA, [2]School of Oceanography, University of Washington, Seattle, WA, USA

Key Points:

- Real-time double-difference (RT-DD) system enables precision monitoring of seismicity at Axial Seamount using the OOI cabled OBS array
- Precise event locations reveal structure and evolution of a mature, outward dipping, convex ring fault system in the shape of a figure 8
- The faults express the complex interaction between volcanic processes at Axial Seamount and sea floor spreading at the Juan der Fuca Ridge

Correspondence to:
F. Waldhauser,
felixw@ldeo.columbia.edu

Citation:
Waldhauser, F., Wilcock, W. S. D., Tolstoy, M., Baillard, C., Tan, Y. J., & Schaff, D. P. (2020). Precision seismic monitoring and analysis at Axial Seamount using a real-time double-difference system. *Journal of Geophysical Research: Solid Earth*, *125*, e2019JB018796. https://doi-org.ezproxy.cul.columbia.edu/10.1029/2019JB018796

Received 2 OCT 2019
Accepted 25 MAR 2020
Accepted article online 6 APR 2020

Abstract Seven three-component ocean bottom seismometers (OBS) of the Ocean Observatories Initiative (OOI) Cabled Array on top of Axial Seamount are continuously streaming data in real time to the Incorporated Research Institutions for Seismology (IRIS). The OBS array records earthquakes from the submarine volcano which last erupted on 24 April 2015, about 4 months after the array came online. The OBS data have proven crucial in providing insight into the volcano structure and dynamics (Wilcock et al., 2016, https://doi-org.ezproxy.cul.columbia.edu/10.1126/science.aah5563). We implemented a real-time double-difference monitoring system that automatically computes high-precision (tens of meters) locations of new earthquakes. The system's underlying double-difference base catalog includes nearly 100,000 earthquakes and was computed using kurtosis phase onset picks, cross-correlation phase delay times, and 3-D *P* and *S* velocity models to predict the data. The relocations reveal the fine-scale structures of long-lived, narrow (<200 m wide), outward dipping, convex faults on the east and west walls of the caldera that appear to form a figure 8-shaped ring fault system. These faults accommodate stresses caused by the inflation of magma prior to and deflation during eruptions. The east fault is segmented and pulled apart in east-west direction due to its interaction with the Juan de Fuca Ridge, which at this location forms an overlapping spreading center. The RT-DD system enables the monitoring and rapid analysis of variations in fine-scale seismic and fault properties and has the potential to improve prediction of timing and location of the next Axial eruption expected to occur in the 2022–2023 time frame.

1. Introduction

The new Ocean Observatories Initiative's (OOI's) cabled array (Kelley et al., 2014) is a state-of-the-art geophysical observatory at Axial Seamount, an active submarine volcano at the intersection of the Juan de Fuca Ridge and the Cobb-Eickelberg seamount chain beneath the Pacific Ocean off the coast of Oregon (Figure 1). The basaltic volcano features a shallow, elongated caldera that is 8.5 km long and 3 km wide and located approximately 1,400 m below the sea surface. It erupted in 1998 (Dziak & Fox, 1999; Fox, 1999, among others), in 2011 (Caress et al., 2012; Chadwick et al., 2012; Dziak et al., 2012), and most recently in April 2015 (Chadwick et al., 2016; Nooner & Chadwick, 2016; Wilcock et al., 2016). The latest eruption was captured by the OOI cabled array, providing high-fidelity geophysical data that led to significant advances in understanding the structure and dynamics of Axial volcano (Caplan-Auerbach et al., 2017; Levy et al., 2018; Nooner & Chadwick, 2016; Tan et al., 2019; Wilcock et al., 2016).

The seismological component of the OOI Cabled Array at the volcano summit consists of five short-period three-component seismometers and two broadband three-component seismometers with hydrophones that started streaming seismic data in real time in November 2014. The network occupies the southern part of the NNW oriented caldera (Figure 1). The array recorded the continuous buildup of seismicity toward the 24 April 2015 eruption, with a peak rate of over 9,000 detected events on the first day of the eruption. Over 100,000 events were detected and located in postprocessing analysis mode using standard analysis methods, revealing segments of a figure 8-shaped ring fault system that accommodated the inflation and deflation of the magma chamber (Wilcock et al., 2016). Furthermore, the network recorded impulsive acoustic signals (Figure 1b) generated when magma reached the seafloor and followed paths that bounced one or more

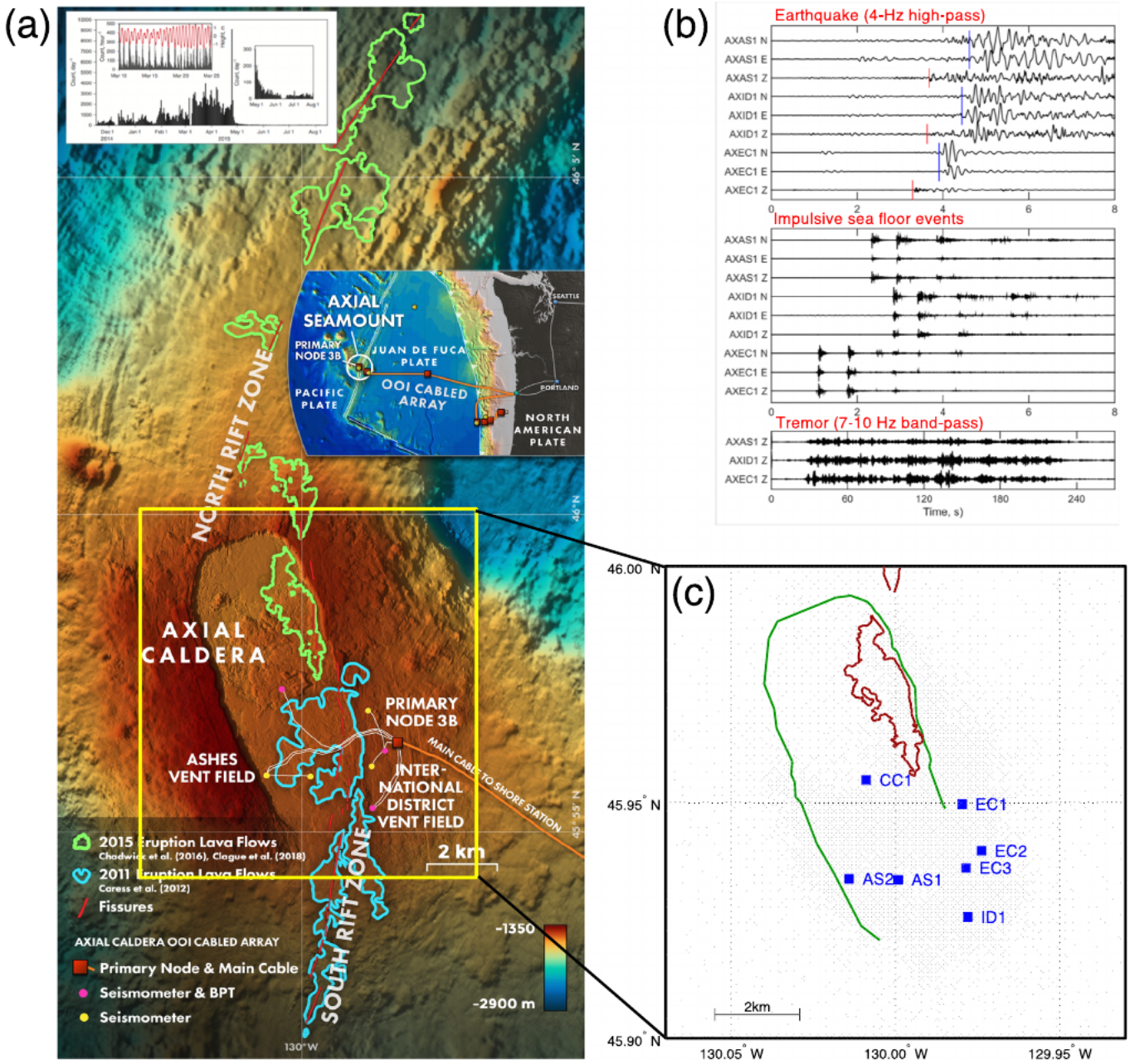

Figure 1. (a) Bathymetry of Axial Seamount showing the configuration of the geophysical instrumentation of the OOI Cabled Array and the location of fissures and lava flows associated with the 2011 (Caress et al., 2012) and 2015 (Chadwick et al., 2016; Clague et al., 2017) eruptions. North and south rift zones are segments of the Juan de Fuca Ridge (from Wilcock et al., 2018). (inset) Histogram of earthquake detections for 9 months spanning the 2015 eruption. Gaps in the histogram are intervals with no data. (b) Examples of the three types of seismic signals recorded by the ocean bottom seismometers (OBS) array: Regular earthquakes due to shear failure, pressure waves from lava reaching the sea surface and exploding or imploding, and long period tremors. Picks for *P* waves (red) and *S* waves (blue) are shown. From Wilcock et al. (2018). (c) Routine locations (gray dots) as determined at the University of Washington by Wilcock et al. (2016) using single-event (Hypoinverse; Klein, 2002) location based on kurtosis *P* and *S* wave picks. Blue, labeled squares are OBS station locations (CC1 and EC2 are broadband stations; all others are short period), green line is the caldera rim, and red lines are lava flow pattern from the 2015 eruption (Clague et al., 2017).

times off the sea surface before reaching the seismometers. These signals were used to precisely map and time lava flow during the eruption and diking event (Wilcock et al., 2016).

Here we present and evaluate the performance of a real-time workflow (Figure 2) that enables precision monitoring of seismicity recorded at the OOI array. We combine a suite of state-of-the-art seismic analysis

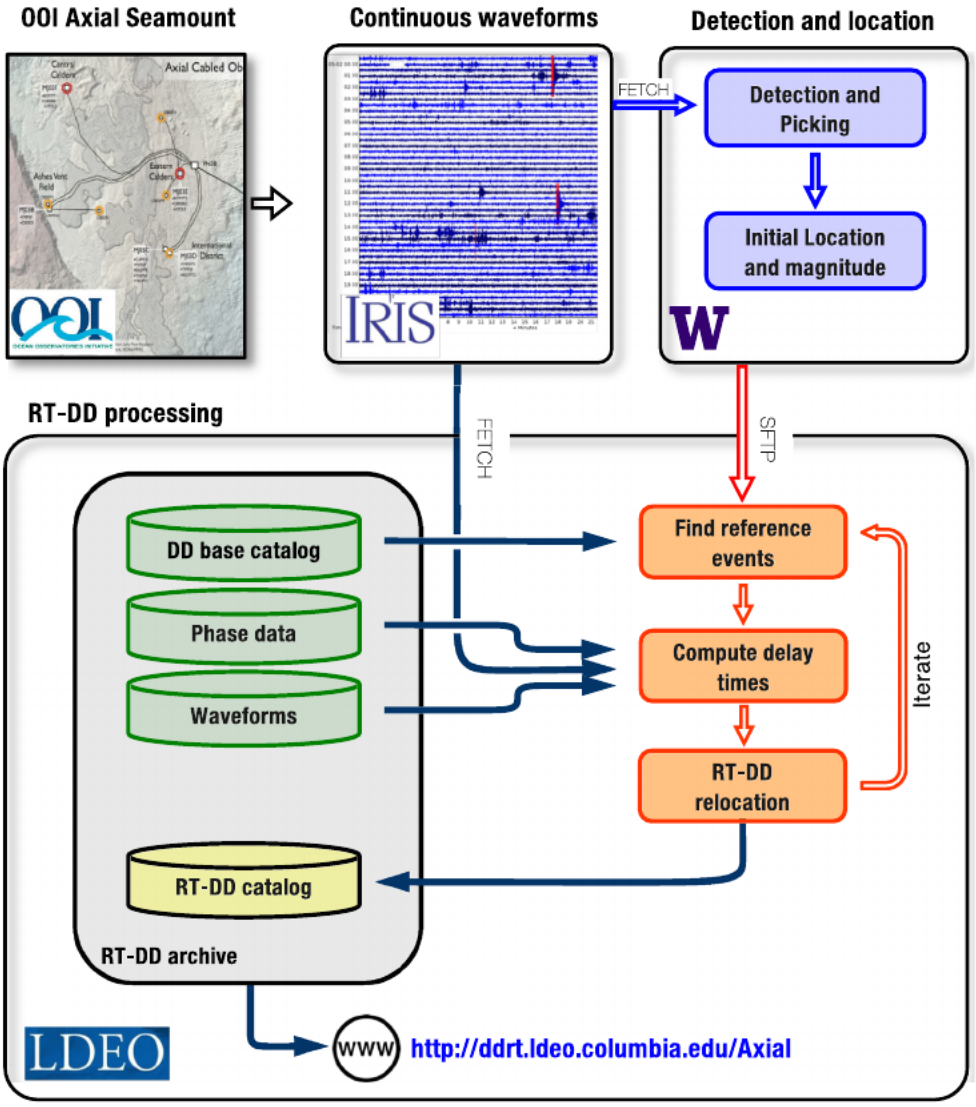

Figure 2. Flowchart of the real-time double-difference (RT-DD) process. Red arrows = process flow; blue arrows = data flow. OOI = Ocean Observatories Initiative; IRIS = Incorporated Research Institute for Seismology; W = University of Washington; LDEO = Lamont-Doherty Earth Observatory of Columbia University. Modified from Waldhauser (2009).

tools to rapidly detect and locate new seismic events at Axial Seamount with high precision relative to a high-resolution background (or base) earthquake catalog. We developed the base catalog by relocating nearly 100,000 events between 22 January 2015 and 31 January 2017 using kurtosis arrival time picks (Baillard et al., 2013; Wilcock et al., 2016) in combination with cross-correlation-based double-difference methods (Waldhauser & Ellsworth, 2000). The base catalog and associated databases are then implemented in the real-time double-difference software system RT-DD (Waldhauser, 2009) for precisely locating new events in a routine monitoring framework. The fine-scale details of the relocated seismicity are analyzed and discussed in terms of the structural and temporal evolution of active faulting during and after the 2015 eruption cycle. We expect the RT-DD system to help improve the forecasting of future eruptions by real-time imaging the fine-scale properties and evolution of active faulting with respect to past seismicity.

2. Data and Methods

2.1. Data and Initial Processing

The OOI array (Kelley et al., 2014) has been streaming three-component data with a sampling rate of 200 Hz since November 2014 through the U.S. NAVY to the Incorporated Research Institute for Seismology (IRIS)

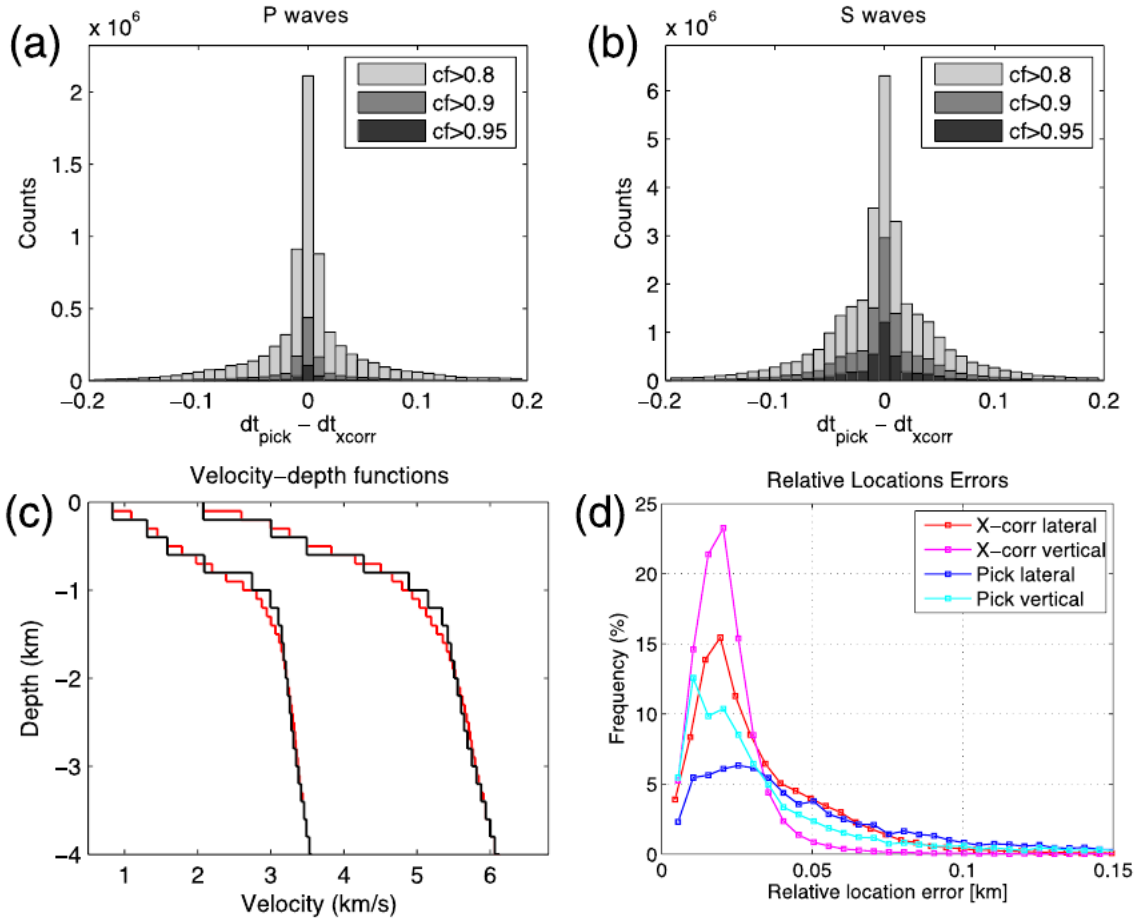

Figure 3. (a, b) Histograms of differences between cross-correlation delay times and corresponding delay times formed from picks for *P* and *S* waves, for different thresholds of correlation coefficients (*Cf*). The standard deviations for correlation coefficients >0.95 are 37 ms for *P* waves and 39 ms for *S* waves. (c) 1-D *P* and *S* velocity models based on Arnulf et al. (2014) used for Hypoinverse location (black lines) and resampled velocity depth function used in HypoDD (red lines). (d) Distribution of the horizontal and vertical projections of the 95% error ellipses derived from bootstrapping the final residuals vector 200 times, for events that lie within the footprint of the array (~75,000 events). Uncertainties are shown separately for events that are mostly constrained by correlation data and those mostly by pick data.

where it is archived at the Data Management Center (DMC). The data can be accessed by the broader scientific community in real time about 75% of the time. About 25% of the time the data are diverted by the U.S. NAVY, with about 90% of that data released to the IRIS data base within a week. Down-sampled 8 Hz data are never diverted to the U.S. NAVY and instead continuously streamed to IRIS all the time and accessible in real time.

We first process the waveforms at the University of Washington using routine analysis methods (Wilcock et al., 2016) that include detection using a long-term (LT)/short term (ST) root-mean-square (RMS) detector operating on 6 and 0.3 s long windows, respectively (Figure 2). After removing signals related to fin whale calls (>15 Hz) and impulsive waterborne signals generated by explosions (or implosions) of lava as they reach the seafloor (Figure 1b) (Wilcock et al., 2016), an ST/LT RMS picker is used to estimate *P* and *S* wave arrivals within 0.15 and 0.2 s long windows. These picks are subsequently refined using the kurtosis picker of Baillard et al. (2013).

Each detected and identified earthquake is subsequently located using Hypoinverse (HINV) (Klein, 2002) together with a layered 1-D model (Figure 3c). The 1-D *P* velocity model is derived from active source data (Arnulf et al., 2014), and the *S* model is derived by scaling the *P* model with a depth dependent V_P/V_S ratio (Wilcock et al., 2016; Figure 1c). We compute magnitudes using the method of Tréhu and Solomon (1983) and Toomey et al. (1985). For a detailed description of the initial data processing steps see Wilcock

Table 1
Number of P and S Picks and Correlation Measurements at Each Station

Station	Picks ($P \geq 4$/P and $S \geq 5$)		X correlation ($n \geq 3$)	
	P	S	P (5 km, cc ≥ 0.7)	S (EHN)
AXAS1	76,734	75,133	1,100,513	1,747,032 (2 km, cc ≥ 0.7)
AXAS2	67,252	59,927	244,254	1,395,050 (2 km, cc ≥ 0.7)
AXCC1	88,855	77,736	1,695,873	598,056 (2 km, cc ≥ 0.7)
AXEC1	97,014	101,161	1,415,924	9,377,371 (1 km, cc ≥ 0.8)
AXEC2	101,470	101,136	1,317,454	7,685,861 (2 km, cc ≥ 0.7)
AXEC3	96,431	101,601	1,508,145	9,845,958 (1 km, cc ≥ 0.8)
AXID1	61,355	48,260	123,829	1,030,420 (2 km, cc ≥ 0.7)

et al. (2016). The initial routine earthquake parameters are made available online via http://axial.ocean.washington.edu (Wilcock et al., 2016).

2.2. 3-D Grid Search Location

In order to improve the absolute location and associated uncertainties of 107,130 hypocenters recorded between January 2015 and January 2017, we relocate them one at a time using a nonlinear grid search method (*NLLoc*, Lomax et al., 2000) together with 3-D P and S velocity models derived from simultaneous inversion of the seismic arrival times from close to 3,900 well recorded earthquakes (Baillard et al., 2019). The velocity models feature a low velocity anomaly in the center of the southern caldera at depths below the top of the magma chamber (~2 km), interpreted as a zone that is intensely fractured by the cyclical deformation of the caldera (Baillard et al., 2019). It further includes high velocities around the caldera rim that are likely due to consolidated undeformed lava flows, and low V_P/V_S ratios in the southern caldera that are consistent with the presence of hydrothermal vapor (e.g., Toksöz, 1976). The median errors of the *NLLoc* hypocenter locations are approximately 500 m in horizontal and 800 m in vertical direction.

2.3. Double-Difference Catalog Relocation

To improve the relative locations between events and image the details in fault structures and geometry, we use the double-difference (DD) method of Waldhauser and Ellsworth (2000). The double-difference method inverts phase delay times between nearby events recorded at common stations for the vector connecting the events, thus reducing common mode model errors. In addition to the phase delay times formed from the kurtosis picks we use waveform cross correlation to compute precise differential times for pairs of events that have correlated seismograms at common stations. We applied a time domain cross-correlation algorithm (Schaff & Waldhauser, 2005) to filtered (4–50 Hz) vertical (EHZ/HHZ) and horizontal (EHE/HHE, EHN/HHN) component seismograms of pairs of events recorded at the same station and separated by at least 1 km. (Table 1). A total of ~10 billion correlations for ~100,000 events were carried out.

We chose 0.5 s long correlation windows for P waves and 0.75 s windows for S waves and search over lags that are ±0.5 s. Erroneous correlation measurement, for example, due to cycle skipping, are detected and removed by computing delay times for a second set of windows that are 0.75 s (P wave) and 1.0 s (S wave) long, retaining only the measurements that agree within 0.01 s. In addition, we keep only the correlation delay times for earthquake pairs with at least three measurements with cross-correlation coefficients, $Cf \geq 0.7$. We use the S delay times measured on the EHN component because they show slightly higher mean correlation coefficients. The resulting correlation time database includes a total of 7 million P wave and 33 million S wave delay times (Table 1). Differences between pick and corresponding correlation delay times have standard deviations of 48 ms (P waves) and 52 ms (S waves) for all data, indicating high consistency between the two data sets (Figures 3a and 3b). Standard deviations of 37 ms (P waves) and 39 ms (S waves) for differences from data with $Cf \geq 0.95$ indicate the high accuracy of the kurtosis picked arrival times, for both P and S arrivals.

We combine pick and the highest quality correlation delay times ($Cf \geq 0.8$) and use the double-difference relocation algorithm HypoDD (Waldhauser, 2001) to invert batches of ~3,000 events (see below) for precise relative locations (Waldhauser & Ellsworth, 2000). We include all events that have at least four P picks and five picks in total and use a finely layered 1-D model (Figure 3c) derived from active source data (Arnulf et al., 2014) to predict partial derivatives and delay times. We tested the consistency between individual data types by relocating a well-constrained cluster of 650 events using picks alone, correlation data alone, and the combined data sets (see Waldhauser & Ellsworth, 2000).

Relative location uncertainties are computed from a bootstrap analysis of the final double-difference vector, relocating the events 200 times while each time resampling the residual vector without replacement (Waldhauser & Ellsworth, 2000). The accuracy of the bootstrap errors is evaluated for small clusters of events using formal least squares uncertainties derived from the full covariance matrix. For events within the array (75,000 events or 77% of the total number of events), the horizontal and vertical projections of the 95%

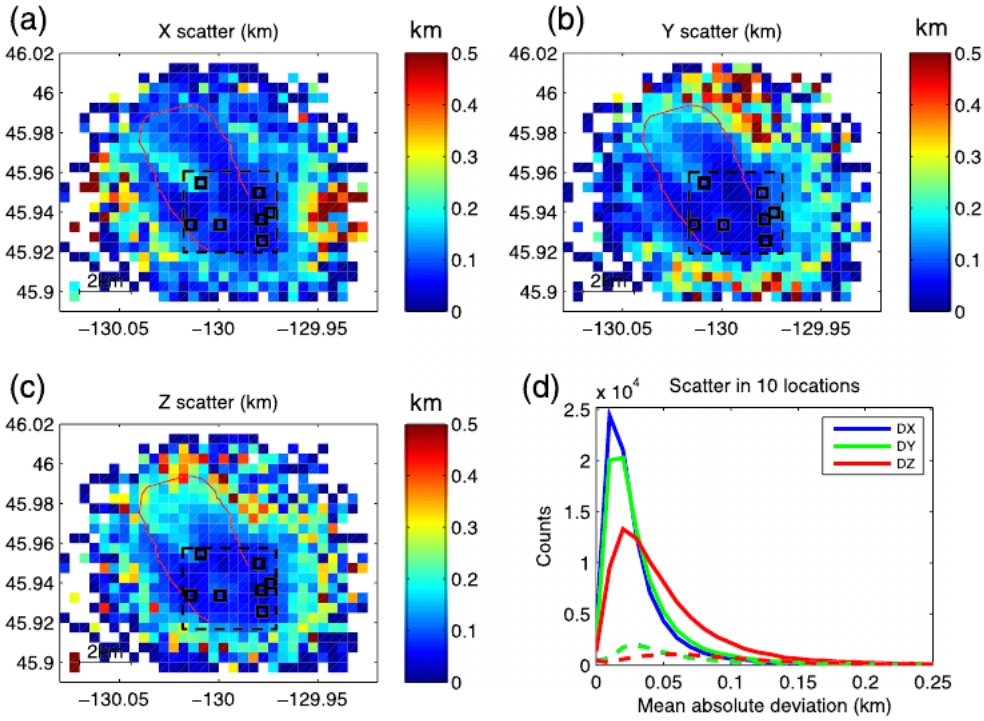

Figure 4. Median absolute deviations (MAD) in the scatter of the 10 locations derived for each event from relocation of randomly sampled subsets of ~3,000 events (300 subsets total). Shown are map views of mean MAD within bins of 500 × 500 m for east-west (a) and north-south (b) directions and depth (c). Black squares are station locations. (d) Histogram of MAD values for all events within the array (i.e., within black boxes in a–c) (solid line) and outside the array (dashed).

confidence ellipses drawn from 200 bootstrap samples have medians of 54 and 30 m, respectively, for events constrained by picks only (~15% of all events) (Figure 3d). Events constrained by additional correlation data have horizontal and vertical medians of 26 and 20 m, respectively. For events located outside the array the error estimates are about 2–3 times larger on average.

We handle the high density of the earthquake distribution, and thus the exponential increase in the number of linear equations to be solved in one inversion, by applying the relocation process described above to randomly subsampled batches of ~3,000 events, each batch encompassing the entire area of seismicity, until the full catalog is relocated. We repeat that process 10 times in order to insure a continuous chain of delay times that link together nearest neighbors across all events. We then merge all batches by taking the mean of the 10 locations for each event to compute a final location. The scatter in the 10 locations, as shown in Figure 4 by the mean of the median in absolute deviations (MAD) within bins of 500 × 500 m for the two lateral directions and depth, is on the order of 40 m within the array. The scatter is about 25% larger for events that locate outside the array because of suboptimal station distribution. The scatter is comparable to the relative location uncertainties derived from the bootstrap analysis for events within the array described above (Figure 3d).

The final catalog, Axial.DD.201701.n5 (Figure 5a), includes 96,706 events (91% of the initial catalog) recorded between 22 January 2015 and 31 January 2017, with magnitudes M_L between −0.8 and 3.1. The final root-mean-square (RMS) residuals are 0.065 s for pick and 0.003 s for cross-correlation delay times. About 75% of the events have at least one correlation measurement with $Cf \geq 0.8$ constraining the final locations.

2.4. Real-Time Double-Difference Monitoring

We implemented a modified version of the real-time double-difference earthquake relocation system RT-DD, originally developed to compute automatic precision location of earthquakes recorded at the Northern California Seismic Network (Waldhauser, 2009). The Northern California RT-DD systems has

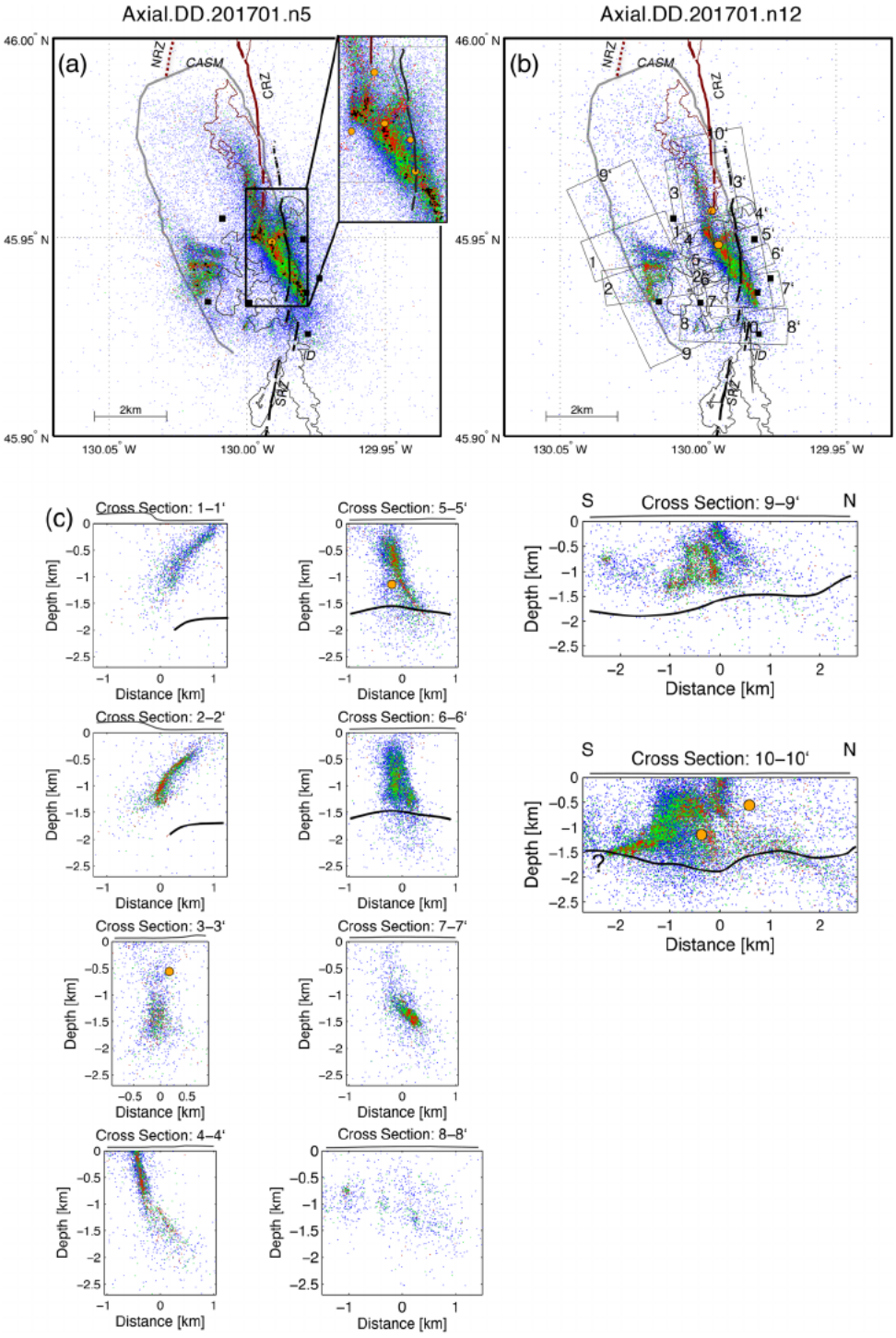

Figure 5. Final cross-correlation-based double-difference earthquake catalogs including events between 22 January 2015 and 31 January 2017. Green dots are correlated events that have at least three seismograms with neighboring events that have correlated *P* waves with coefficients ≥0.95, red dots are strongly correlated events with coefficients ≥0.98, blue dots all other events. Orange dots are events with $M_L \geq 3.0$. (a) Map view of comprehensive catalog including 96,706 events relocated with at least four *P* wave picks and at least five picks in total. Black squares show station locations, gray line caldera outline, and thick (thin) brown and black lines fissures (lava flows) of 2015 (Chadwick et al., 2016; Clague et al., 2017) and 2011 (Caress et al., 2012) eruptions, respectively. Dotted brown line marks southward trajectory of the NRZ (see Figure 1). NRZ = north rift zone; SRZ = south rift zone. CRZ = central rift zone; ID = International District vent field. Box shows location of inset. Black dots show locations of repeating events. (b) Map view and (c) cross sections of high-precision catalog including 31,160 events located with at least seven high-quality *P* wave picks and at least 12 picks in total, used as base catalog for RT-DD processing. Labeled boxes in (b) show the location of cross sections shown in (c). Black lines above surface in (c) show bathymetry, at depth top of magma reservoir (Arnulf et al., 2018).

Table 2
Back-Testing Results for 2,000 Randomly Selected Events Using the Axial.DD.201701.n12 and Axial.DD.201701.n5 as Base Catalogs

	DX mean	DY mean	DZ mean	DX median	DY median	DZ median
N12	122	137	216	55	50	114
N5	148	177	248	68	76	131

Note. Mean and median difference between DD base catalog locations and RT-DD location are given in meters.

been operational since 2009 and continues to provide a widely used, openly accessible, up-to-date correlation-based double-difference catalog and web-based tools to view and analyze new earthquakes relative to past seismicity (http://ddrt.ldeo.columbia.edu).

The RT-DD system uses a DD base catalog to rapidly compute high-precision locations of new events relative to their nearest neighbors in the base catalog. For each newly detected and located event (http://axial.ocean.washington.edu, Wilcock et al., 2016), the RT-DD process searches for neighboring reference events in the base catalog, computes pick delay times between the new event and its reference events, and uses a single-event DD algorithm to relocate the new event with respect to the reference events in the base catalog (Waldhauser, 2009). It subsequently uses the new location to search the base catalog for a new set of optimal reference events, this time cross-correlating the waveforms between the new event and its reference events to compute precise differential times. Waveforms from the reference events are accessed from a locally stored indexed waveform database. Waveforms for new events are retrieved from IRIS DMC using *FetchData*, requesting windows that start 2 s before and end 12 s after the initial origin time estimate. The final RT-DD relocation is performed with the combination of both pick and correlation times. A detailed description of the RT-DD system is given in Waldhauser (2009).

The DD catalog described above (Axial.DD.201701.n5) was computed with the aim of being comprehensive (i.e., requiring a minimum number of five stations for robust relocation). However, for real-time DD operation it is most useful to include events in the base catalog that are recorded by many stations and have additional *S* picks in order to ensure strong linkage between new and reference events in the base catalog. To generate the base catalog for the Axial-RT-DD system, we have therefore repeated the catalog relocation process described above but this time only including events that have at least 7 *P* wave picks (i.e., events recorded at all stations) and 12 picks in total. We also added all events with $M > 2$, regardless of the number of picks available. The relocated catalog, Axial.DD.201701.n12, includes 31,160 events with magnitudes M_L between −0.6 and 3.1 (Figures 5b and 5c). RMS residuals are 0.064 s for pick data and 0.002 s for correlation data, and the relative horizontal and vertical location uncertainties from bootstrap analysis have medians of 17 and 16 m, respectively (means are 76 and 47 m, respectively). This represents 35% lateral and 20% vertical location error reductions compared to the comprehensive DD catalog. Eighty-five percent of events in the comprehensive and 70% in the well-constrained catalog have correlated seismograms at $Cf \geq 0.8$.

We back tested the RT-DD process by relocating 2,000 randomly selected events between 2015 and 2016 from the DD base catalog (Axial.DD.201701.n12), treating them as new events and then comparing them to their catalog location. The mean difference between the base catalog location and the RT-DD location is 137 m in horizontal directions (median 55 m) and 216 m in vertical direction (median 114 m). These differences are about 20% smaller than when the full catalog (Axial.DD.201701.n5) is used as base catalog (Table 2). The origin of the discrepancies between base catalog and real-time locations lies in the comprehensive linkage between events in the simultaneous inversion of the data used to compute the base catalog. In contrast, the RT-DD process only inverts delay times between new events and a selected number (200) of reference events in the base catalog. Continuous RT-DD monitoring will improve location precision of future events.

Figure 6 shows the difference between the HINV initial locations and the RT-DD relocations, for 4,540 events between 1 February 2017 until 5 May 2018. Standard deviations are 270 and 370 m in the east-west and north-south directions, respectively, and 458 m in depth, similar to the expected absolute location uncertainties of the HINV locations. We observe a mean shift of 137 m for differences in east-west direction, which originates from referencing the RT-DD solutions to a base catalog derived in a 3-D tomographic model that accounts for velocity heterogeneities (Baillard et al., 2019), whereas the routine HINV locations are based on a 1-D model (Figure 3c).

With the RT-DD system operational, we are now continuously updating the Axial DD catalog with precise locations of new events in near-real time (http://ddrt.ldeo.columbia.edu/Axial). Figure 7 shows an example of a summary information plot that is routinely being generated and put online for each new event. In addition to station and earthquake location information we also provide tools to investigate each new location in

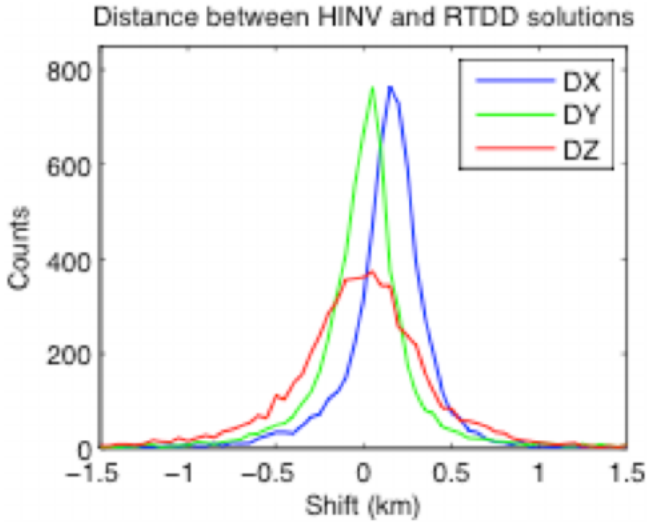

Figure 6. Differences between routine HINV locations of 4,300 events that occurred after the end of the base catalog and corresponding RT-DD locations that were automatically computed using the initial HINV location as starting location for RT-DD processing. Standard deviations (means) are 270 m (140 m) in east-west, 360 m (10 m) in north-south, and 450 m (30 m) in vertical direction.

space and time with a JavaScript-based 4-D earthquake viewer (http://ddrt.ldeo.columbia.edu/Axial/4D). Plots with new waveforms and waveforms from the 10 most correlated neighboring events (Figure 7c) are also generated and posted online, providing additional information on both source and structural characteristics related to each new earthquake.

3. Results

3.1. Structures and Faults

The overall structure and geometry of the faults revealed by the relocated seismicity (Figure 5) is generally consistent with the features observed by Wilcock et al. (2016). These include active faults along the eastern and western caldera walls that form part of what appears to be an outward dipping ring fault system in the shape of a figure 8 and seismicity associated with fissures of the 2015 diking event. The faults reach depths that correspond to the top of the magma reservoir (~1.6 km; Arnulf et al., 2018). Approximately 85% of the earthquakes that are within the footprint of the network locate above 1.6 km depth, and 90% locate above 2 km.

Earthquake density plots (Figure 8) reveal the focused occurrence of earthquakes along narrow zones of faulting, especially along the east caldera wall. ENE oriented cross sections (3–5) depict the outward dipping faults that accommodate the stresses from inflation and deflation of the caldera during the eruption. Upon scrutinizing the shallow portion of the eastern fault in Cross Section 4 we see some indication of a steeply inward dipping fault that splays off the eastern ring fault at about 200 m depth and reaches the surface near the caldera east wall, a structure proposed by Baillard et al. (2019). However, reliably resolving shallow inward dipping faults with the current network configuration is hampered by the low resolution in hypocenter depths due to the near-horizontal ray take-off angles. In both our initial 3-D grid search locations (Baillard et al., 2019) and the double-difference locations presented here we do not see evidence of an active shallow, inward dipping fault along the northern caldera's west wall (Figure 5c, Cross Section 1) as inferred by Arnulf et al. (2018). However, such a structure, if it exists, would be difficult to constrain with the current network given the events' large azimuthal gaps (>250°) and near-horizontal take-off angles.

The seismicity on the west wall defines a convex, west dipping fault surface with a subtle change in strike at the neck of the figure 8 structure, and an overall decreasing dip toward the surface (1 and 2 of Figure 5). A principal component analysis (PCA) was used to fit fault planes to events along the two cross sections. The resulting planes' orientation were generally consistent with focal mechanisms from Levy et al., 2018 and indicate that the northern segment of the western ring fault (Cross Section 1 in Figure 5) strikes 24°NNW and dips 65°WSW, while the southern segment (Cross Section 2) strikes 8°NNW and dips 55°WSW. Approximately 90% of the events are within 300 m from the PCA-derived fault planes, and 30% are within the resolution limits of the data (~50 m) (Figure 9a). Most of the seismic moment is released within 300 m from the fault plane (Figure 9b) which is similar to observations along mature crustal faults like the Parkfield segment of the San Andreas fault (Perrin et al., 2019).

Seismicity on the east side of the caldera reflects the complex interaction of the eastern ring fault with the NNE trending Juan de Fuca Ridge, which at this location steps to the west by about 2 km, forming the northern, central, and southern rift zones of an overlapping spreading center (OSC) (Embley et al., 1990) (Figures 1 and 5b). Cross Sections 4 and 5 in Figure 5c show a steeply outward dipping ring fault, which is bounded to the north (Cross Section 3) and south (Cross Section 6) by seismicity which we interpret to be associated with rifting processes along fissures of the Juan de Fuca Ridge (for location of the fissures see Figures 1 and 5). PCA results from the eastern ring fault segments show fault orientations of ~25°NNW and a steep decline in the number of events and moment as a function of distance from the PCA plane. Most of the seismic moment is released within 150 m from the fault plane, suggesting a well-developed fault core bracketed by a narrow damage zone. The existence of a well-developed fault surface is also supported by the sharp alignment of strongly correlated events (red dots in Sections 4 and 5),

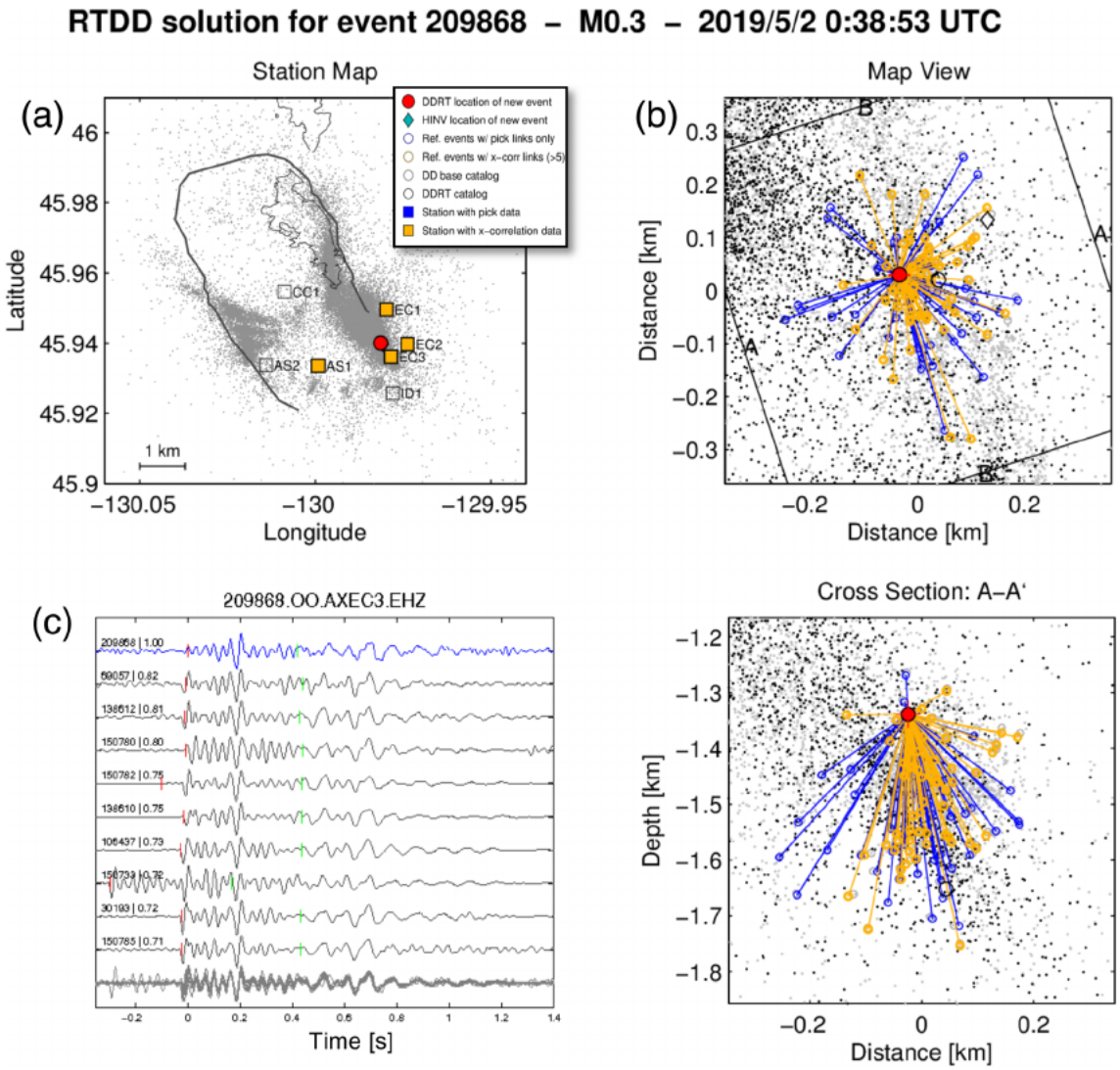

Figure 7. Example information for each relocated new event generated by the RT-DD system and posted online at http://ddrt.ldeo.columbia.edu/Axial. (a) Station map with OBS locations (squares), events in base catalog (gray dots), new event (red dot), caldera wall (black line), and 2015 lava flow areas (gray lines). (b) Map view (top) and cross section (bottom) of area with new event, showing base catalog (gray dots), past RT-DD located events (black dots), new event (red dot). Blue lines connect new event to reference events constrained by pick data alone, yellow lines to events constraint by correlation data. (c) Waveform plot of 10 most similar seismograms (gray) recorded at station EC3, aligned on correlated *P* waves. Filter: 4–50 Hz. Top (blue) trace is new event, bottom trace is superposition of all seismograms. Red/green ticks are kurtosis-based *P*/*S* wave arrival time picks. Labels indicate event ID and correlation coefficient.

suggesting repeated slip on a single fault. Inspection of larger preeruption events with the 4-D viewer suggests that the basic ring fault geometry along the caldera's east side is a mirrored version of that observed on the west side but has been deformed, or may have undergone segmentation, due to the interacting rift segments. The structural complexity near the neck of the figure 8 structure is also reflected in the low number of correlated events at this location (Figure 5a, inset).

Seismicity associated with the central rift zone (Figure 8, Sections 1 and 2) forms a linear, NNW trending structure that veers off the east wall of the caldera in the general direction of the observed surface fissures generated by the 2015 eruption (Chadwick et al., 2016; Clague et al., 2017; Wilcock et al., 2016). These earthquakes form a diffuse, near-vertical structure between 1.0 and 1.8 km depth, but the constraint on both absolute and relative event locations, especially in depth, is limited because of the large azimuthal gap in the stations recoding the events (Figure 4).

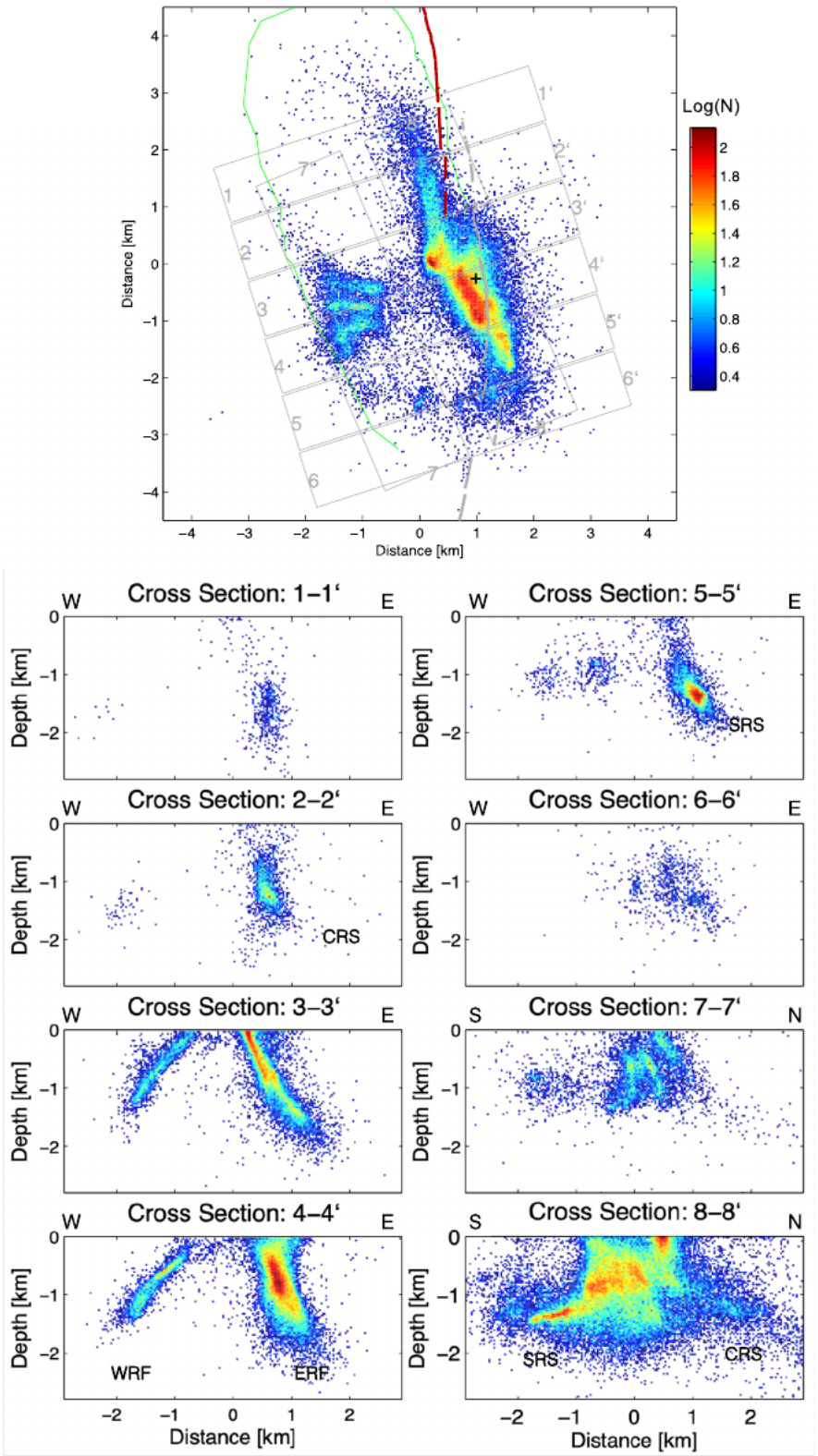

Figure 8. Map view and cross sections of earthquake densities within bins of 30 × 30 m, shown on a logarithmic scale. In map view, green line is caldera rim, brown lines are 2015 fissures, dark gray lines are 2011 fissures, labeled boxes include events shown in cross sections. WRF = western ring fault; ERF = eastern ring fault; CRS = central rift segment; SRS = south rift segment. The "+" denotes the centroid of the best fitting prolate spheroid deformation model (Nooner & Chadwick, 2016).

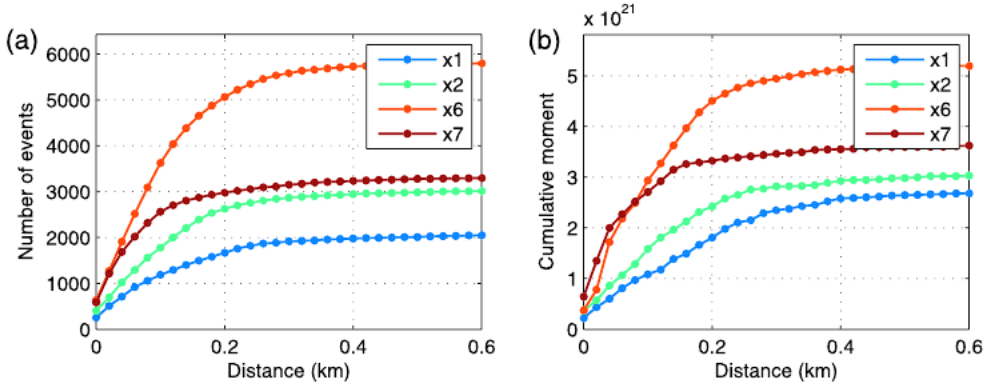

Figure 9. Cumulative number of events (a) and moment (b) within bins of 20 m from four fault planes derived from a principal component analysis of events along the west wall (x1, x2) and the east wall (x6, x7). Labels in legend correspond to cross sections shown in Figure 5 (see also Cross Sections 3 and 4 in Figure 8).

Seismicity along the south rift zone trends in NNW direction (Figure 5b), veering off the general NNE direction of the surface fissures toward the south. At depth the events concentrate between 1 and 1.6 km depth and show an east dipping structure (Section 7 in Figure 5c) with decreasing dip toward the south. The surface projections of the seismic structure track the 2011 surface fissures.

A series of short, NNE striking, subparallel faults in the southernmost part of the ring structure (Figure 5b and Cross Section 8 in Figure 5c) run perpendicular to a strike that we would expect from movements on the ring fault. Composite focal mechanisms (Levy et al., 2018) indicate right-lateral dip-slip movement along a nodal plane that is consistent with the orientation of the seismicity structure. These structures are subparallel to surface fissures in the south rift zone associated with the 2011 eruption (Figure 1a) and the general trend of the Juan de Fuca Ridge, suggesting that they are the response to stress concentration from interacting rifting processes. They may also be related to the hydrothermal systems in the International District area (Figure 1) or result from a combination of both processes.

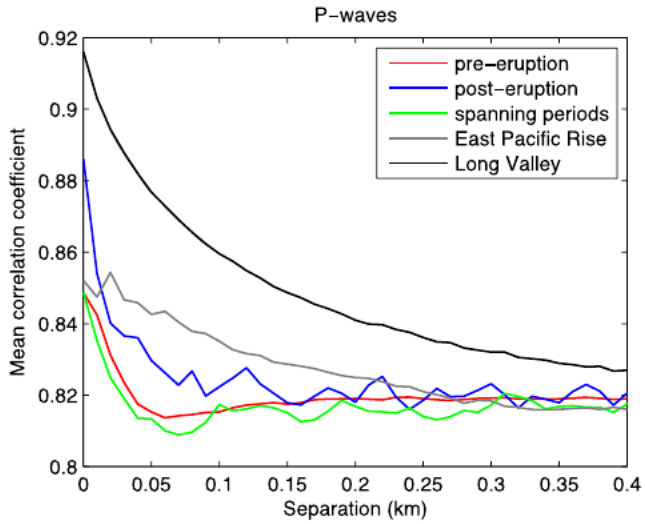

Figure 10. Mean *P* wave correlation coefficients (*Cf*) as a function of hypocenter separation, shown for pairs of events where both events occurred before the eruption, after the eruption, and for events that span to two time periods. Mean values are calculated within bins of 10 m separation distances, for pairs that were recorded by at least four stations. Correlation coefficients between 0.7 and 1.0 are used. Measurements from the East Pacific Rise at 9°50′N (Waldhauser & Tolstoy, 2011) and Long Valley caldera (Waldhauser & Schaff, 2008) are also shown for comparison.

3.2. Cross-Correlation Coefficients

Areas of high event density (Figure 8) correlate, to a first degree, with areas that have large numbers of correlated events (events with at least three *P* waves with $Cf > 0.95$, green dots, and $Cf > 0.98$, red dots in Figure 5). When earthquakes locate in close proximity to each other, their waves travel along identical paths and thus create similar seismograms at common stations. Waveform similarity typically decays with increasing distance between hypocenters as a result of increasing variation in velocity structures along the wave paths and variation in source characteristics. The more complex the tectonic setting (i.e., the shorter the wavelength of velocity variations), the faster the decay with increasing hypocenter separation. Furthermore, waveforms decorrelate even for colocated sources when the velocity structure between sources and receiver changes between the times of recording.

Figure 10 shows the distribution of *P* wave correlation coefficients as a function of hypocenter separation, averaged within bins of 10 m, for pairs of events that have at least four *P* wave correlation measurements. Curves are shown for event pairs that occur before the eruption, after the eruption, and for pairs with events spanning the two periods. All three curves rapidly flatten out at $Cf \sim 0.82$ beyond just 75 m separation distance, indicating a strongly heterogenous velocity structure. Decorrelation occurs much faster at Axial compared to

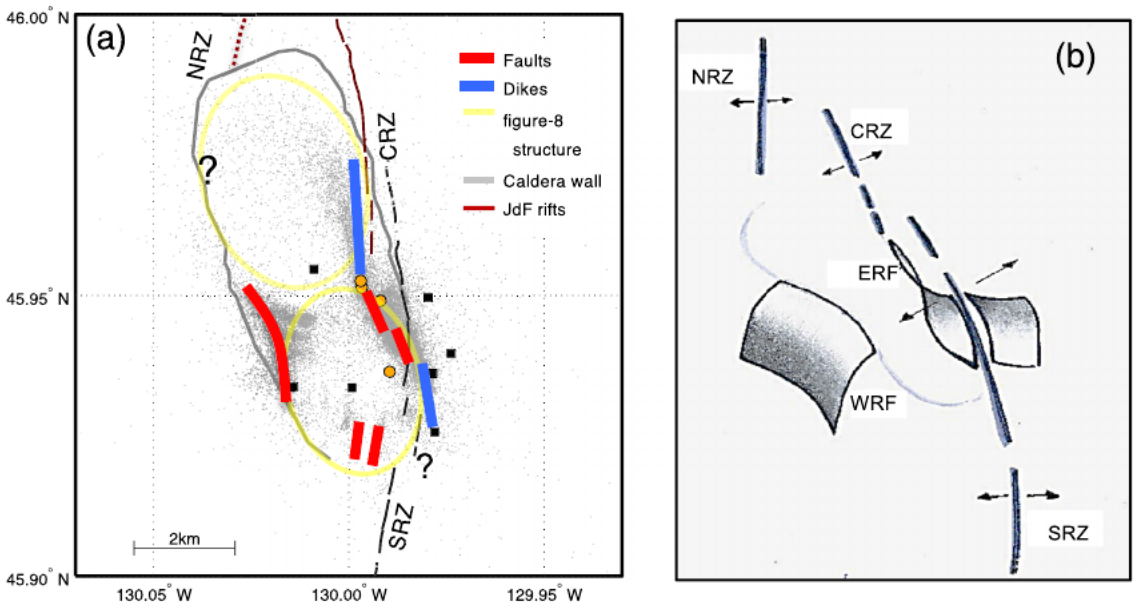

Figure 11. (a) Summary of observations, showing the main faults and dikes inferred from the relocated seismicity and mapped fissures. Gray dots are earthquakes, black squares seismic stations. (b) Simplified perspective sketch (looking north) of location and geometry of active faults and dikes. NRZ = north rift zone; SRZ = south rift zone; CRZ = central rift zone; ERF = eastern ring fault; WRF = western ring fault.

other volcanic regions such as the Long Valley caldera in California (Waldhauser & Schaff, 2008) and similar measurements from the East Pacific Rise where seismicity is driven by a combination of volcanic, tectonic, and hydrothermal processes (Waldhauser & Tolstoy, 2011) (Figure 10).

Furthermore, Figure 10 shows that changes in structural and/or source specific heterogeneities are time dependent. Earthquakes during the preeruption period (red line) show lower correlation coefficients than posteruption earthquakes (blue line), consistent with the eruption being preceded by changes in the velocity field due to rising magma and complex source processes, especially for small events that dominate the correlation coefficients shown in Figure 10. Significantly lower correlation coefficients are observed between events that span the two periods. Levy et al. (2018) show that prior to eruption vertical uplift of the caldera floor was accommodated by normal faulting events on the ring faults. Events of reversed slip direction occurred during the coeruption and posteruption period as the caldera floor subsided. This change in source characteristics is reflected in the lower correlation coefficients for event pairs spanning the two periods.

We searched for repeating events, earthquakes that rupture the same fault area with sources of similar magnitude and mechanism, following the procedure described in Waldhauser and Ellsworth (2002), and found 71 sequences with up to three events. Events within each of these sequences colocate and have highly correlated seismograms. All repeating event sequences are only active prior to the eruption and locate on both sides of the caldera (black dots in Figure 5a). All first events in the most robust sequences occur within a 10-day period, and the second events occur in a narrow time period as well, an indication that timing might be modulated by some transient effect. The existence of repeating earthquakes suggests that the short-wavelength fault geometry is robust and likely developed through several eruption cycles. This is consistent with the generally narrow (~250 m) width of the active fault zones at Axial (Figure 9).

4. Discussion

The relocation results provide detailed images in time and space of the active parts of a NNW oriented, outward dipping, figure 8-shaped ring fault system and intersecting ridge structures. A simplified depiction of the seismically active zones and sketch summarizing the general structure of Axial Seamount are given in Figure 11. Discrimination between ring fault and dike-related seismicity is based on their location relative to surface features as well as their temporal evolution during the 2015 eruption (see below). Faults near

the neck of the figure 8 structure are convexly curved to accommodate the change in strike of the faults that accommodated magma inflation and deflation during the 2015 eruption at Axial Seamount (Levy et al., 2018; Wilcock et al., 2016). The seismically active fault zones are narrow and smooth, suggesting that the ring faults are mature and well-developed and therefore were likely active during previous eruptions. These eruptions were all sourced along the eastern margin of the magma chamber (Chadwick et al., 2016; Nooner & Chadwick, 2016), with dikes propagating along the south rift in 1998 and 2011 and along the central and north rift in 2015, which define the OSC (Embley et al., 1990).

The NNE trending north rift intersects the caldera at its northern end at the site of the Canadian American Seamount (CASM) vent field (Figures 1 and 5a). The central rift segment, which sidesteps the north rift to the east and curves from north to NNW, intersects the eastern caldera wall just north of the neck of the figure 8 structure. At this location, the northern terminus of the NNE trending south rift is located about 1 km to the east of the central rift segment. The south rift segment interacts with the eastern caldera wall in the southern part of the caldera (Figure 5). The overall structure of seismicity and seafloor observations (bathymetry, fissures, and hydrothermal vents) image the interaction between the OSC's central and southern segments with the structure of Axial volcano. The eastern ring fault is caught between the two overlapping rift segments and is being pulled apart by ongoing rifting processes (Figure 11).

Preeruption event density (Figure 12a) is highest along the east caldera wall in an area of high inflation as revealed by bottom pressure data (Nooner & Chadwick, 2016). Peak density of 500 events within 100 × 100 m bins were recorded over the 3 month period from 22 January to 23 April 2015 along the east wall, compared to 200 lower-magnitude events along the west wall. A break in seismic density near the neck of the figure 8 caldera structure (black arrow in Figure 12a) supports the idea of a segmented eastern ring fault. The three main active structures on the eastern side of the caldera, that is, the central and south rifts and the (segmented) east wall (Figure 11), all experienced a pickup in seismicity since the start of monitoring in January 2015. Decreasing event rates at the end of March 2015 were followed by a period of accelerated event rates until the day of the eruption (histogram in Figure 12a). Earthquakes occur mostly in bursts, activating distinct parts of the eastern ring fault (e.g., starting on 29 January 2015 at 22:09:00), the central rift zone (30 January 2015 at 03:19:00) and the south rift zone (8 February 2015 at 16:19:00) (see https://ddrt.ldeo.columbia.edu/Axial/4D). It appears that these structures are activated independently and are not synchronized, until the start of vigorous activity around 24 April 2015 at 06:10:00 that spreads across the entire volcano and indicates magma ascending within dikes.

As observed by Wilcock et al. (2016), the seismicity first starts to migrate south along the south rift at about 06:10:00 on 4 April. However, events abruptly stop migrating southward at the beginning of the eruption and turn northward along the central rift segment, bridging the gap that existed in the preeruption seismicity (Figure 12a). Less than 2 hr after the onset of the seismic crisis, at 08:01, lava erupts along the central rift fissures (Caplan-Auerbach et al., 2017; Wilcock et al., 2016) and seismicity migrates at a speed of 0.55 m/s first north along the central rift. Outside of the detection capability of the seismic array, mapped fissures indicate that the dike stepped westward to the north rift, representing the propagation of a dike that coincides with the rapid onset of deflation (Nooner & Chadwick, 2016; Wilcock et al., 2016).

Using data from the 1975–1984 Krafla rifting episode, Buck et al. (2006) demonstrated that dike intrusions change the tectonic stress field so that subsequent dikes may propagate different directions than the previous dike, with diminishing lengths of propagation. However, the short interval (~4 years) with respect to the previous Axial eruption (Wilcock et al., 2018) may also play an important role due to lack of time for stress to build up at the site of the previous diking, whereas the previous two eruptions with a gap of ~13 years between them both propagated to the south. Furthermore, magma supply from reservoirs in the north of Axial caldera may have played a role in controlling rifting direction in 2015 (Arnulf et al., 2018).

The 20 month long posteruption activity from 22 May 2015 to the end of the base catalog (31 January 2017) concentrates on the east wall of the caldera, with a distribution similar to the syneruption seismicity, although at a much lower rate (peak density of 25 events per 100 × 100 m over 20 months). An isolated area at the southeastern edge of the caldera that was not active during the eruption is activated posteruption (black arrow in Figures 12c and 12d). Virtually no earthquakes were detected along the west wall during the same time period. The west wall became active again 2 years after the eruption (Figure 13).

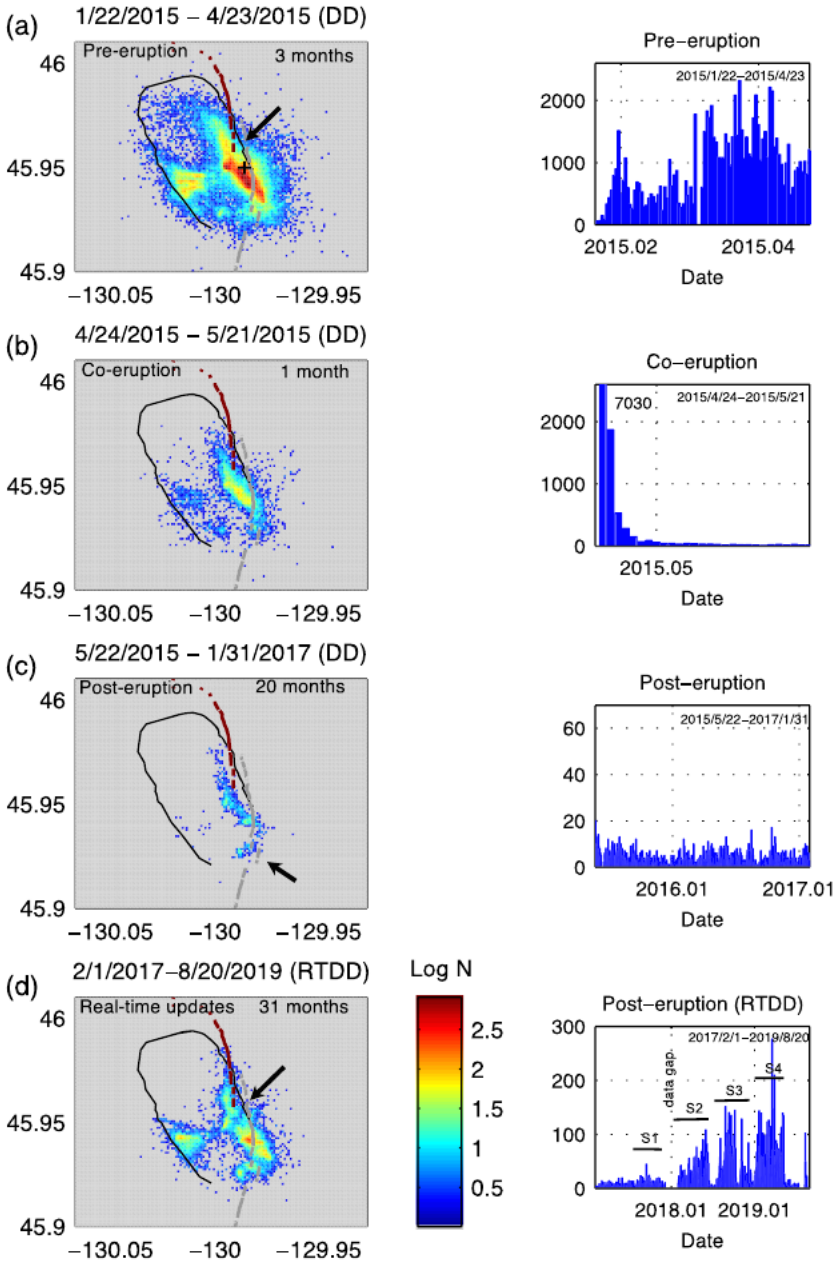

Figure 12. Evolution of event densities within bins of 50 × 50 m. (a) Events in the 3 months leading up to the eruption in April 2015, (b) in the 1 month during the eruption, (c) in the subsequent 20 months after the eruption until the end of the DD base catalog (Axial.RTDD.201701.n5), and (d) in the 31 months since the start of real-time double-difference (RT-DD) processing. In (a) the maximum number per bin is capped at 300 to improve visibility of density distribution (highest density bin has 500 events). Black line is caldera rim, brown and gray lines are fissures associated with the 2015 and 2011 eruptions, respectively (Clague et al., 2017). Right panels = histograms of daily event counts. Labels in histogram (d) refer to Figure 13.

An increase in the number of recorded events is observed since the beginning of 2018. The events occur in bursts, with four increasing active bursts that can be identified during our observational period: September 2017 (50 events/day), May 2018 (110 events/day), September 2018 (150 events/day), and March 2019 (280 events/day). Most of these events reactivate sections of the fault system that were previously active, with density plots beginning to show the same patterns, including the seismicity gap on the eastern ring fault, as during the 2015 preeruption period (Figure 13d).

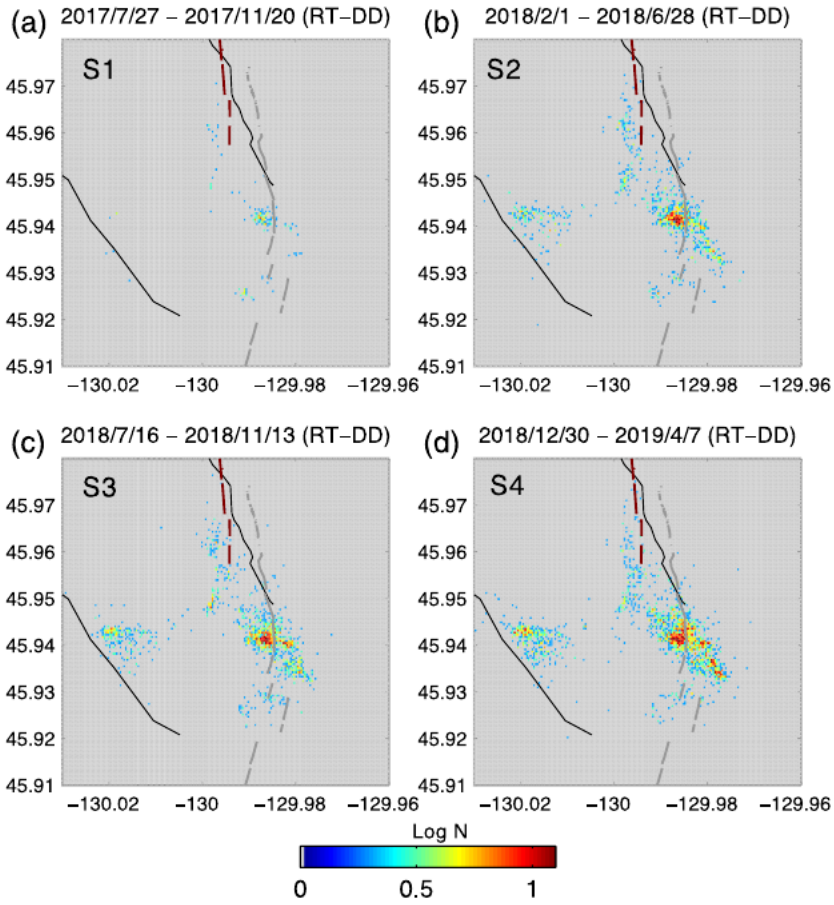

Figure 13. Event density maps within 50 × 50 m for periods S1–S4 indicated in the histogram of Figure 12d. Black line is caldera rim, brown and gray lines are fissures associated with the 2015 and 2011 eruptions, respectively (Clague et al., 2017).

Since the beginning of the posteruption period, real-time differential deformation data have shown a steady, long-term rate of inflation, albeit with some pauses (https://www.pmel.noaa.gov/eoi/rsn/Forecasts.html), that point to an inflation recovery in ~April 2021 and an eruption within about a year from then (Chadwick et al., 2012; Nooner & Chadwick, 2016). Seismicity rates are expected to increase as well. The new monitoring system of detecting, associating, and locating at the University of Washington followed by RT-DD processing at the Lamont-Doherty Earth Observatory will be able to keep up with computing precise locations during peak seismicity rates of 2,000 day^{-1} that we expect during an eruption (Wilcock et al., 2016). We therefore will be able to track and analyze, with respect to baseline characteristics from previous eruptions, the evolution of seismic activity leading up to the eruption in real time, providing the scientific community with fundamental high-resolution data that have the potential to predict location and timing of magma ascent and eventual eruption.

5. Conclusions

Using real-time data from the OOI Cabled array at Axial Seamount, we implemented an automatic real-time double-difference procedure that updates a high-precision earthquake catalog within tens of seconds after a new event occurs. The results are immediately made available online at http://ddrt.ldeo.columbia.edu/Axial, together with web-based, interactive tools for viewing and analyzing the seismicity in time and space. The precision catalog for nearly 100,000 events since January 2015 developed in this study serves as background reference for the real-time solutions and at the same time provide insight into the fine-scale structure and evolution of a long-lived ring fault system as it interacts with diking processes along segments of an OSC

of the Juan de Fuca Ridge. Real-time information from the Axial RT-DD system is now being used to monitor the structure and evolution of active faults and dykes as well as changes in seismic activity relative to baseline characteristics. Together with other data from cabled OOI instruments, they provide critical information that has the potential to lead to informed decisions about the state of stress and timing of the next eruption, as well as the geographic scope of the eruption as it is occurring.

Acknowledgments
The seismic data used for this study are archived at the Incorporated Research Institutions for Seismology Data Management System (http://ds.iris.edu/gmap/#network=OO&planet=earth) and the Ocean Observatories Initiative (OOI) Data Portal (https://oceanobservatories.org/cabled-array-seismometer-data/). Results from this study are made available automatically and in near-real time at http://ddrt.ldeo.columbia.edu/Axial. We thank the OOI and IRIS for making the real-time and archived seismic data available and easily accessible. We thank Michael West and Jackie Caplan-Auerbach for thorough and constructive reviews that helped improve the manuscript, Suzanne Carbotte and Adrian Arnulf for discussions and sharing their results, and Eric Malikowski for help with developing the 4D viewer. This work was supported by NSF-OCE Grants 1536320 (F. W., M. T., Y. J. T., and D. S.) and 1536219 (W. W. and C. B.). The seismic network was installed and is operated by the OOI Cabled Array team, led by J. Delaney and D. Kelley. This is LDEO Contribution Number 8385.

References

Arnulf, A. F., Harding, A. J., Kent, G. M., Carbotte, S. M., Canales, J. P., & Nedimović, M. R. (2014). Anatomy of an active submarine volcano. *Geology*, *42*(8), 655–658. https://doi-org.ezproxy.cul.columbia.edu/10.1130/G35629.1

Arnulf, A. F., Harding, A. J., Kent, G. M., & Wilcock, W. S. D. (2018). Structure, seismicity, and accretionary processes at the hot spot-influenced axial seamount on the Juan de Fuca Ridge. *Journal of Geophysical Research: Solid Earth*, *123*, 4618–4646. https://doi-org.ezproxy.cul.c 10.1029/2017JB015131

Baillard, C., Crawford, W. C., Ballu, V., Hibert, C., & Mangeney, A. (2013). An automatic kurtosis-based *P*-and *S*-phase picker designed for local seismic networks. *Bulletin of the Seismological Society of America*, *104*(1), 394–409. https://doi-org.ezproxy.cul.columbia.edu/10.1785/012013

Baillard, C., Wilcock, W. S. D., Arnulf, A. F., Tolstoy, M., & Waldhauser, F. (2019). A joint inversion for three-dimensional *P*- and *S*-wave velocity structure and earthquake locations beneath Axial Seamount. *Journal of Geophysical Research: Solid Earth*, *124*, 12,997–13,020. https://doi-org.ezproxy.cul.columbia.edu/10.1029/2019JB017970

Buck, W. R., Einarsson, P., & Brandsdottir, B. (2006). Tectonic stress and magma chamber size as controls on dike propagation: Constraints from the 1975–1984 Krafla rifting episode. *Journal of Geophysical Research*, *111*, B12404. https://doi-org.ezproxy.cul.columbia.edu/10.1029/2005J

Caplan-Auerbach, J., Dziak, R. P., Haxel, J., Bohnenstiehl, D. R., & Garcia, C. (2017). Explosive processes during the 2015 eruption of Axial Seamount, as recorded by seafloor hydrophones. *Geochemistry, Geophysics, Geosystems*, *18*, 1761–1774. https://doi-org.ezproxy.cul.columbia.edu/1 2016GC006734

Caress, D. W., Clague, D. A., Paduan, J. B., Martin, J., Dreyer, B., Chadwick, W. W. Jr., et al. (2012). Repeat bathymetric surveys at 1-metre resolution of lava flows erupted at Axial Seamount in April 2011. *Nature Geoscience*, *5*(7), 483–488. https://doi-org.ezproxy.cul.columbia.edu/10.1

Chadwick, W. W., Nooner, S. L., Butterfield, D. A., & Lilley, M. D. (2012). Seafloor deformation and forecasts of the April 2011 eruption at Axial Seamount. *Nature Geoscience*, *5*(7), 474–477. https://doi-org.ezproxy.cul.columbia.edu/10.1038/ngeo1464

Chadwick, W. W. Jr., Paduan, J. B., Clague, D. A., Dreyer, B. M., Merle, S. G., Bobbitt, A. M., et al. (2016). Voluminous eruption from a zoned magma body after an increase in supply rate at Axial Seamount. *Geophysical Research Letters*, *43*, 12,063–12,070. https://doi.org/10.1002/2016GL071327

Clague, D. A., Paduan, J. B., Caress, D. W., Chadwick, W. W. Jr., Le Saout, M., Dreyer, B. M., & Portner, R. A. (2017). High-resolution AUV mapping and targeted ROV observations of three historical lava flows at Axial Seamount. *Oceanography*, *30*(4), 40–57.

Dziak, R. P., & Fox, C. G. (1999). The January 1998 earthquake swarm at Axial volcano, Juan de Fuca Ridge: Hydroacoustic evidence of seafloor volcanic activity. *Geophysical Research Letters*, *26*(23), 3429–3432. https://doi-org.ezproxy.cul.columbia.edu/10.1029/1999GL002332

Dziak, R. P., Haxel, J. H., Bohnenstiehl, D. R., Chadwick, W. W., Nooner, S. L., Fowler, M. J., et al. (2012). Seismic precursors and magma ascent before the April 2011 eruption at Axial Seamount. *Nature Geoscience*, *5*(7), 478–482. https://doi-org.ezproxy.cul.columbia.edu/10.1038/ng

Embley, R. W., Murphy, K. M., & Fox, C. G. (1990). High resolution studies of the summit of Axial volcano. *Journal of Geophysical Research*, *95*, 12,785–12,812.

Fox, C. G. (1999). In situ ground deformation measurements from the summit of Axial volcano during the 1998 volcanic episode. *Geophysical Research Letters*, *26*(23), 3437–3440. https://doi-org.ezproxy.cul.columbia.edu/10.1029/1999GL900491

Kelley, D. S., Delaney, J. R., & Juniper, S. K. (2014). Establishing a new era of submarine volcanic observatories: Cabling Axial Seamount and the Endeavour segment of the Juan de Fuca Ridge. *Marine Geology*, *352*, 426–450. https://doi-org.ezproxy.cul.columbia.edu/10.1016/j.margeo

Klein, F. W. (2002). User's guide to HYPOINVERSE2000, a Fortran program to solve for earthquake locations and magnitudes. U.S. Geological Survey Open-File Report, 02-172, 123 pp.

Levy, S., Bohnenstiehl, D. R., Sprinkle, P., Boettcher, M. S., Wilcock, W. S. D., Tolstoy, M., & Waldhauser, F. (2018). Mechanics of fault reactivation before, during, and after the 2015 eruption of Axial Seamount. *Geology*, *46*(5), 447–450. https://doi-org.ezproxy.cul.columbia.edu/10.11

Lomax, A., Virieux, J., Volant, P., & Berge, C. (2000). Probabilistic earthquake location in 3D and layered models: Introduction of a Metropolis-Gibbs method and comparison with linear locations. In C. H. Thurber, & N. Rabinowitz (Eds.), *Advances in seismic event location* (pp. 101–134). Amsterdam: Elseiver.

Nooner, S. L., & Chadwick, W. W. Jr. (2016). Inflation-predictable behavior and co-eruption deformation at Axial Seamount. *Science*, *354*(6318), 1399–1403. https://doi-org.ezproxy.cul.columbia.edu/10.1126/science.aah4666

Perrin, C., Waldhauser, F., Choi, E., & Scholz, C. (2019). Persistent fine-scale fault structure and rupture development: A new twist in the Parkfield, California, story. *Earth and Planetary Science Letters*, *521*, 128–138. https://doi.org/10.1016/j.epsl.2019.06.010

Schaff, D. P., & Waldhauser, F. (2005). Waveform cross-correlation-based differential travel-time measurements at the Northern California Seismic Network. *Bulletin of the Seismological Society of America*, *95*, 2446–2461.

Tan, Y. J., Waldhauser, F., Tolstoy, M., & Wilcock, W. S. D. (2019). Axial Seamount: Periodic tidal loading reveals stress dependence of the earthquake size distribution (*b* value). *Earth and Planetary Science Letters*, *512*, 39–45. https://doi-org.ezproxy.cul.columbia.edu/10.1016/j.epsl.2019

Toksöz, M. N. (1976). Velocities of seismic waves in porous rocks. *Geophysics*, *41*(4), 621. https://doi-org.ezproxy.cul.columbia.edu/10.1190/1.1440639

Toomey, D. R., Solomon, S. C., Purdy, G. M., & Murray, M. H. (1985). Microearthquakes beneath the median valley of the mid-Atlantic ridge near 23°N: Hypocenters and focal mechanisms. *Journal of Geophysical Research*, *90*, 5443–5458.

Tréhu, A. M., & Solomon, S. C. (1983). Earthquakes in the Orozco transform zone: Seismicity, source mechanisms, and tectonics. *Journal of Geophysical Research*, *88*(B10), 8203–8225. https://doi-org.ezproxy.cul.columbia.edu/10.1029/JB088iB10p08203

Waldhauser, F. (2001), HypoDD: A computer program to compute double-difference earthquake locations. *U.S. Geol. Surv. Open File Rep.* 01-113, Menlo Park, CAL

Waldhauser, F. (2009). Near-real-time double-difference event location using long-term seismic archives, with application to Northern California. *Bulletin of the Seismological Society of America*, *99*, 2736–2848. https://doi-org.ezproxy.cul.columbia.edu/10.1785/0120080294

Waldhauser, F., & Ellsworth, W. L. (2000). A double-difference earthquake location algorithm: Method and application to the northern Hayward Fault, California. *Bulletin of the Seismological Society of America*, *90*(6), 1353–1368. https://doi-org.ezproxy.cul.columbia.edu/10.1785/012

Waldhauser, F., & Ellsworth, W. L. (2002). Fault structure and mechanics of the Hayward Fault, California, from double-difference earthquake locations. *Journal of Geophysical Research*, *107*(B3), 2054. https://doi-org.ezproxy.cul.columbia.edu/10.1029/2000JB000084

Waldhauser, F., & Schaff, D. P. (2008). Large-scale relocation of two decades of Northern California seismicity using cross-correlation and double-difference methods. *Journal of Geophysical Research*, *113*, B08311. https://doi-org.ezproxy.cul.columbia.edu/10.1029/2007JB005479

Waldhauser, F., & Tolstoy, M. (2011). Seismogenic structure and processes associated with magma inflation and hydrothermal circulation beneath the East Pacific Rise at 9°50'N. *Geochemistry, Geophysics, Geosystems*, *12*, Q08T10. https://doi-org.ezproxy.cul.columbia.edu/10.1029/2011C

Wilcock, W. S. D., Dziak, R. P., Tolstoy, M., Chadwick, W. W. Jr., Nooner, S. L., Bohnenstiehl, D. R., et al. (2018). The recent volcanic history of Axial Seamount: Geophysical insights into past eruption dynamics with an eye toward enhanced observations of future eruptions. *Oceanography*, *31*(1), 114–123. https://doi-org.ezproxy.cul.columbia.edu/10.5670/oceanog.2018.117

Wilcock, W. S. D., Tolstoy, M., Waldhauser, F., Garcia, C., Tan, Y. J., Bohnenstiehl, D. R., et al. (2016). Seismic constraints on caldera dynamics from the 2015 Axial Seamount eruption. *Science*, *354*(6318), 1395–1399. https://doi-org.ezproxy.cul.columbia.edu/10.1126/science.aah556